RSC Advances

Designable Fabrication of Hierarchical $WO_3·H_2O$ Hollow Microspheres for Enhanced Visible Light Photocatalysis

Sheng-Qi Guo,[a] Meng-Meng Zhen,[a] Mei-Qing Sun,[a] Xiao Zhang,[a] Ya-Ping Zhao,[*b] Lu Liu[*a]

[a] *Tianjin Key Laboratory of Environmental Remediation and Pollution Control, Nankai University, Tianjin 300071, China.*

[b] *Department of Environmental Science, East China Normal University, Shanghai 200241, China.*

KEYWORDS: $WO_3·H_2O$ · green chemistry · hierarchical structure · hollow microspheres · visible light photocatalytic

Author information

* Corresponding author.

E-mail: ypzhao@des.ecnu.edu.cn; liul@nankai.edu.cn.

Abstract: The synthesis controlled via morphology of $WO_3{\cdot}H_2O$ nanostructures has been prepared through a facile hydrothermal route. $WO_3{\cdot}H_2O$ nanoplates with the thickness of ~45 nm and hierarchical hollow microspheres (HMSs) structures could be obtained through introducing different amount of citric acid. X-ray diffraction (XRD), scanning electron microscopy (SEM), and transmission electron microscopy (TEM) were employed to clarify the structure and morphology of the two kinds of $WO_3{\cdot}H_2O$. The formation mechanisms of the $WO_3{\cdot}H_2O$ nanoplates and $WO_3{\cdot}H_2O$ HMSs were investigated. The photocatalytic activities determined by rhodamine B (RhB) degradation under visible light irradiation of $WO_3{\cdot}H_2O$ HMSs photocatalysts were significantly improved as compared with $WO_3{\cdot}H_2O$ nanoplates. The higher efficiency of photocatalytic activity in $WO_3{\cdot}H_2O$ HMSs was attributed to its higher surface-to-volume ratio and stability against aggregation. In addition, we investigated the toxicity of $WO_3{\cdot}H_2O$ HMSs against the important model fungus, yeast (*Saccharomyces cerevisiae*). The results indicate that the as-synthesized hierarchical $WO_3{\cdot}H_2O$ HMSs could be used as green and efficient photocatalyst.

1. Introduction

In modern chemistry and materials science, the precise architectural manipulation of crystals with well-defined morphologies remains a research focus and a challenging issue.[1,2] In particular, the morphology controllable synthesis of inorganic nanomaterials with hierarchical structure has drawn great attention due to their strongly determined physical properties for optical, magnetic, electrochemical and gas sensing properties.[3-7] To date, several excellent reviews about hierarchical structures in natural science have been published following a summary compilation by Waller in 1976.[8-10] The analysis of data for existing materials reveals that hierarchical structure materials, particularly hollow architecture, which possess dual or multiple morphologies and structures, are of great importance for improving performance and further realizing wide potential applications.[11-16] In the past decade, Lou[17-19] and Xie[20,21] groups reported a series of hierarchical hollow architecture nanomaterials, which exhibited fascinating morphology and excellent performance in supercapacitive. In addition, our group committed to synthesis of hierarchical hollow architectures nanomaterials and obtained some achievements.[22,23] Thus far, various chemical routes, including template-assisted method[24-27] (hard and soft template), template-free[28-31] (Ostwald ripening process, Kirkendall effect, or chemically induced self-transformation), have been developed to assemble hierarchical hollow architectures. However, rationally manipulating the morphology and architecture of inorganic materials in solution remains a challenge for material design.

Tungsten oxide is known as a multifunctional material with electrochromic, optochromic, and gasochromic properties.[32] As we know that the valuable functions greatly depend on the size and structure.[33,34] Thus, tungsten oxide with controlled morphologies has become favorable due to their unique properties. In the past few years, much effort has been made to synthesize tungsten oxide, and the nano- and micro-sized tungsten trioxide (WO_3) with different morphologies had been obtained in succession.[35-39] Among of them, the majority are based on nanoparticles, nanosheets, nanotube arrays and nanofibers *etc*. However, examples of hierarchical structure, especially hierarchical hollow architectures, are extremely rare, which have been strongly motivated because of their unique properties of low effective density, high specific surface area, and good permeation.

As shown above, it is a great challenge to control synthesis the WO_3 hollow architecture with hierarchical structure. Here, we report a facile way to synthesize $WO_3 \cdot H_2O$ nanoplates with thickness of about 40 to 50 nm. By controlling the reaction conditions, we can also fabricate hierarchical hollow microspheres (HMSs) of $WO_3 \cdot H_2O$ from its nanoplates. The proposed formation mechanisms of the $WO_3 \cdot H_2O$ HMSs have been investigated. Our design of $WO_3 \cdot H_2O$ HMSs is also instructive and meaningful to the synthesis of other inorganic nanomaterials with hierarchical structures. In addition, photocatalytic performances of the as-prepared $WO_3 \cdot H_2O$ are investigated, the photocatalytic activity of $WO_3 \cdot H_2O$ HMSs was significantly higher than $WO_3 \cdot H_2O$ nanoplates.

2. Experimental Section

Material Characterization.

X-ray diffraction analysis of the samples were carried out by an X-ray diffractometer (XRD, Rigaka D/max2500) with Cu Kα radiation (λ = 1.54056 Å). The morphology of the as-prepared products was characterized by scanning electron microscopy (SEM, Hitachi-530 or JEOLJSM-6700F) and transmission electron microscopy (TEM, JEOL-2010, operating voltage of 200 kV). The Brunauer−Emmett−Teller (BET) specific surface area (SBET) of the sample was analyzed by nitrogen adsorption in a Tristar 3000 nitrogen adsorption apparatus. UV spectra were recorded on a Cary 5000 spectrometer at room temperature. Fluorescence spectrum was characterized by RPM2000.

Preparation of $WO_3·H_2O$ nanoplates.

$WO_3·H_2O$ nanoplates were prepared via a facile hydrothermal method, and all reagents are of analytic grade and were used without further purification. In a typical synthesis, a mixture of $Na_2WO_4·2H_2O$ (0.3g), citric acid (0.3g) in H_2O (25ml) was adjusted to pH 1.0 with HCl stirred for 30 min, and then sealed in a 30ml Teflon-lined stainless steel autoclave and heated at 100°C for 10 h. After the sample was gradually cooled to room temperature, a yellow precipitate was collected and then washed with distilled water and absolute ethanol, and the sample was kept in absolute ethanol.

Preparation of Hierarchical $WO_3·H_2O$ Hollow Microspheres (HMSs).

Hierarchical $WO_3·H_2O$ (HMSs) was prepared in the same way as that for $WO_3·H_2O$ nanoplates but increasing the amount of citric acid from 0.3g to 0.6g.

Photocatalytic Reactions. The photocatalytic activities of the as-prepared hierarchical $WO_3·H_2O$ HMSs were evaluated by the photocatalytic degradation of RhB aqueous solution at room temperature under visible light irradiation. A 500 W Xe lamp with a 420 nm cutoff filter was used as a light source to provide the visible light. In a typical reaction, 0.05 g of as-prepared photocatalysts was dispersed into 50 mL of RhB aqueous solution (1×10^{-5} M). The photodegradation reaction was stopped at 1 hour intervals and 10 mL of reaction solutions were extracted to determine the concentrations of the aqueous RhB solution by UV/vis spectroscopy. In this study, $WO_3{\cdot}H_2O$ nanoplates were used as a reference catalyst to photocatalytic RhB under the same condition as the as-prepared samples. RhB aqueous solution without photocatalysts irradiated by visible light was used as a blank experiment and the as-prepared photocatalysts reacting with RhB in dark were used as comparative evaluation.

Preparation of $WO_3{\cdot}H_2O$ stock solutions

The solutions of synthesized $WO_3{\cdot}H_2O$ nanoplates and HMSs were prepared in YPD medium with the initial concentration of 10000 ppm, respectively. The stock solution was then sonicated for 30 min (AS3120, Autoscience, China) and 2-fold diluted by fresh YPD medium, obtaining the following concentrations of $WO_3{\cdot}H_2O$ nanomaterials, 20, 40, 80, 160, 320, 640, 1280 mg/L.

Growth inhibition assay

The *Saccharomyces cerevisiae* strain InvSc1 (Invitrogen, USA) was used to test the inhibition activity of the two kinds of $WO_3{\cdot}H_2O$ nanomaterials. Growth inhibition by the nanomaterials was tested in glass tubes (a volume of 20 mL). Overnight cultured yeast cells were suspended in fresh YPD medium to an optical density at 600 nm (OD_{600}) of 0.2. 1 mL of cell suspension was added into each tube. Then, 1 mL of the prepared $WO_3{\cdot}H_2O$ solutions with different concentrations were added into the tubes, obtaining 2 mL of the mixtures containing yeast cells with OD_{600} of 0.1 and $WO_3{\cdot}H_2O$ with the following concentrations, 0, 10, 20, 40, 80, 160, 320, 640 and 1280 mg/L. The tubes were incubated with shaking at 30°C for 12 h. Cells in each tube were counted with haemocytometers, and the percent of growth (% Growth) was calculated as the cell number of each treatment group divided by that of the control (without $WO_3{\cdot}H_2O$ treatment) × 100.

Cell viability assay

The viability of treated cells was tested by FDA staining. Cell suspensions after treatment of $WO_3{\cdot}H_2O$ nanomaterials were stained with 2 μL FDA (1 mg/mL, dissolved in acetone, Sigma, USA) for 5 min, washed with PBS buffer and subsequently observed by fluorescence microscope (BX-41, Olympus, Japan) with the green filter set.

3. Results and Discussion

Morphology, characterization, and formation mechanism

The phase structure of the obtained product was first investigated by X-ray diffraction (XRD). As shown in Figure 1d, it can be seen that the XRD pattern is in conformity with orthorhombic $WO_3{\cdot}H_2O$ in space group Pmnb (62) (a= 5.238 Å, b= 10.704 Å, c= 5.12 Å, JCPDS: 43-0679). The observed peaks of $WO_3{\cdot}H_2O$ could be correspond to diffraction from (020), (111), (002), (042) and (222) faces. No characteristic peak was observed for other impurities such as W, WO_3 and $WO_3{\cdot}0.33H_2O$. Interestingly, from Figure 1d, it can also be found that relative diffraction intensities of (020) or (111) face to (002) face is around almost 4 times higher than the corresponding conventional values (JCPDS: 43-0679). This observation indicates that $WO_3{\cdot}H_2O$ sample has special growth orientations, therefore, their (020) and (111) faces tend to be preferentially oriented parallel to the surface of the supporting substrate in the experiment.

Figure 1a and 1b display typical scanning electron microscopy (SEM) images of the as-synthesized products. It's clear that such as-prepared $WO_3{\cdot}H_2O$ samples are composed of a large quantity of nanoplates. The thickness of each nanoplate is around 40 to 50 nm, as revealed from the cross section of those nanoplates standing up on their edges. The high-resolution TEM image of single nanoplate shows that the crystalline lattice distances in the white frame is 3.73 Å (Figure 1c), corresponding to the (120) face of orthorhombic $WO_3{\cdot}H_2O$, which is consistent with the XRD results. Furthermore, the N_2 physisorption isotherm for the sample is a typical type III isotherm based on the Brunauer–Deming–Deming–Teller (BDDT) classification (Figure S1). The BET surface area is 14.01 m^2g^{-1}, and the pore-size distribution curve obtained through the BJH method suggests that majority of pores were ~20 nm in diameter.

/Insert Figure 1/

Generally, the final morphology of crystal was controlled by the nature of crystal structure during the initial nucleation and subsequent Ostwald ripening through the delicate affect of external factors, examples of the additive, concentration, reaction time and so on.[40] Herein, we first considered the influence of nature crystal structure for determining final morphology of nanomaterials. For orthorhombic $WO_3{\cdot}H_2O$, it is built on a layered perovskite-like ReO_3 structure,[41] which in turn governs its growth and facilitates the formation of nanoplates. According to previous report,[36] WO_3 hydrate are all composed of a network of WO_6 octahedra (Figure 2a), and each WO_6 octahedra sharing four *ac* plane O atoms with four neighbors to form a 2D layer plane, which can be described as a $4^4{\cdot}6^2$ net in the *ac* plane (Figure 2b). The 2D layer plane stack along the *b*-axis and are held together *via* intermolecular hydrogen bond (O–H/O) interactions to generate a 3D cube structure (Figure 2c). This means that $WO_3{\cdot}H_2O$ breaks easily along the *b*-axis, and thus readily tends to form plate-like shapes under proper conditions. After $WO_3{\cdot}H_2O$ nanoplates were obtained, we focus on the controlled formation of $WO_3{\cdot}H_2O$ for creating a well organized hierarchical structure, which has been favored for improved application performance. As far as we know, crystallization process of heterogeneous nucleation will leads to the preformed nanoplates aggregate together.[42] Therefore, we adopted the strategy of concentration control to procure the assembly of preformed isolation nanoplates, specific measures is to increase the concentration of a particular reactant. When doubling the concentration of citric acid, a hierarchical $WO_3{\cdot}H_2O$ HMSs structure is obtained successfully.

/Insert Figure 2/

As shown in Figure 3a and 3b, it's clear that such hierarchical $WO_3{\cdot}H_2O$ aggregates constituted by numerous nanoplates with the thickness of ~45 nm. Figure 3c and 3d show typical transmission electron microscopy (TEM) images of $WO_3{\cdot}H_2O$ microspheres, which clearly indicate that $WO_3{\cdot}H_2O$ are hollow microspheres structure and further confirm that the samples are composed of aggregated nanoplates. The XRD pattern in Figure 3e identifies such hierarchical $WO_3{\cdot}H_2O$ as pure $WO_3{\cdot}H_2O$ (JCPDS: 43-0679), similar to that of $WO_3{\cdot}H_2O$ nanoplates. As for porosity, the N_2 adsorption/desorption isotherms for the sample is a typical type IV isotherm with H1 hysteresis loop, which is the characteristic isotherm of mesoporous materials. The BET surface area reaches 23.21 m^2g^{-1}, and the average pore size was calculated as ~14 nm, which may arise from the piled nanoplates and microspheres (Figure 3f).

/Insert Figure 3/

A possible reason why the higher citric acid concentration brought tremendous change on morphology can be explained as followed. It is well known that formation process of crystals tends to be affected by secondary bond of organic molecules deposited on the crystals surface, including hydrogen bonding interaction and van der Waals forces.[43] At the nanoscale, hydrogen bonding has been confirmed to initiate the aggregation of nanoparticles functionalized with hydrogen-bonding ligands, in which the regularity and degree of aggregation depends on the quantity and strength of individual hydrogen bonds.[44,45] For this system, strong acidity environment provide powerful support for hydrogen bonding interactions. Hydrogen-bond attraction and van der Waals electrostatic repulsion are achieving balance under the original concentration of the reactants, and this allows $WO_3{\cdot}H_2O$ nanoplates exist independently. However, increasing concentration of citric acid breaks the balance between the hydrogen-bond interactions and repulsive electrostatic interactions. Plenty of carboxyl and hydroxyl groups make hydrogen-bond attraction become dominant, and result in a strong tendency to get together $WO_3{\cdot}H_2O$ nanoplates under low pH conditions. From macro perspective, dispersed nanoplates assembly together, then hierarchical $WO_3{\cdot}H_2O$ HMSs structure is obtained. As observed in Figure 4a-e, with increasing concentration of citric acid, the degree of aggregation of $WO_3{\cdot}H_2O$ nanoplates significantly increased. These results proved that the formation of hierarchical $WO_3{\cdot}H_2O$ HMSs structure was attributed to the increased hydrogen bonding interaction. Moreover, when citric acid was replaced by other polycarboxy ligands, such as propanedioic acid or EDTA, with keeping the other conditions the same as those of $WO_3{\cdot}H_2O$ nanoplates, no $WO_3{\cdot}H_2O$ products could be obtained (Figure S2). This further suggests that citric acid is important to the formation of $WO_3{\cdot}H_2O$ nanostructures during the hydrothermal process.

/Insert Figure 4/

To further study the formation process of the hierarchical $WO_3{\cdot}H_2O$ HMSs, we conducted time-dependent experiments with different synthetic times from 1 to 10 h, whereas the amount of reactants and reaction temperature were fixed. From the XRD patterns in Figure 5d, it is clearly observed that the formation of $WO_3{\cdot}H_2O$ is very fast after reacting for just 1 h. And the products collected at every time interval are almost consistent with the product obtained at 10 h. However, there is no regular shape product collected at the initial 1 h reaction (Figure 5a). A few well-structured hollow microspheres were formed at 2 h (Figure 5b). Prolonging reaction time to 4 h, more and more hollow microspheres were produced but there exists some damaged microspheres and irregular shape product as observed (Figure 5c). As the reaction proceeds to 10 h, the typical hollow microspheres have been formed. This investigation revealed that the reaction time was also a key parameter in the synthesis of the $WO_3{\cdot}H_2O$ HMSs.

/Insert Figure 5/

Photoelectrochemical properties

The optical properties of hierarchical $WO_3{\cdot}H_2O$ HMSs and simple nanoplates have been investigated by UV-Vis diffuse reflectance spectra (DRS) and photoluminescence (PL) measurements. It can be seen from figure 6a that all the samples exhibit strong visible light absorption with absorption edges at around 550 nm. Compared with simple nanoplates, the absorbance of $WO_3{\cdot}H_2O$ HMSs is enhanced in the range of 400–800 nm, this fact is a key factor for higher photocatalytic activity in the visible light region. In addition, both two samples possessed steep edges in the profile, meaning that the visible light absorption were not caused by the transition from the impurity level but were due to the band gap transition. The band gap energy (Eg) for two $WO_3{\cdot}H_2O$ samples can be estimated from the intercept of the tangents to the plots of $(Ahv)^{1/2}$ vs. photon energy as shown in Figure S3. In this system, the calculated Eg value for $WO_3{\cdot}H_2O$ HMSs and $WO_3{\cdot}H_2O$ nanoplates were 2.22 and 2.3 eV, respectively, which agrees well with previous report for $WO_3{\cdot}H_2O$.[46]

Figure 6b shows the PL emission spectra of two as-prepared samples under excitation at 370 nm. From figure known that the both two samples show wide-band emissions in white range with a peak plat around 550 nm. It can be probably used as white lighting. The change in the PL intensity should be probably associated with the variation of the structure of the nanoplates. Furthermore, the peak intensity of $WO_3{\cdot}H_2O$ HMSs is stronger than that of all the $WO_3{\cdot}H_2O$ nanoplates samples, revealing that the separation rate of electron–hole pairs on $WO_3{\cdot}H_2O$ nanoplates samples is lower than $WO_3{\cdot}H_2O$ HMSs. In general, the interface charge separation efficiency and inhibited of photogenerated electrons and holes recombination are benefit for enhanced photocatalytic activity, so the above test results also signify that $WO_3{\cdot}H_2O$ HMSs have a better photocatalytic performance than $WO_3{\cdot}H_2O$ nanoplates.

/Insert Figure 6/

In order to further validate that the electron–hole pairs were easily separated and transferred to the surface of $WO_3{\cdot}H_2O$ HMSs under visible light irradiation, the electrochemical impendence spectroscopy (EIS) were determined. The EIS spectra were completed using potential amplitude of 5 mV over a frequency range of 0.1-10^6 Hz and were simulated using the *Zview* software. As shown in Figure 7, the diameter of the arc radius for $WO_3{\cdot}H_2O$ HMSs is smaller than that for the $WO_3{\cdot}H_2O$ nanoplates electrode under visible light irradiation, which indicated higher efficiency and more rapid of charge transfer. This result powerful proved that change the morphology from single nanoplates to hierarchical HMSs for $WO_3{\cdot}H_2O$ can dramatically enhance the separation and transfer efficiency of photogenerated electron–hole pairs.

/Insert Figure 7/

Photogradation of RhB in Aqueous Solution.

Through the above photoelectrochemical analysis, we speculated that the $WO_3{\cdot}H_2O$ HMSs have a better photocatalytic performance than $WO_3{\cdot}H_2O$ nanoplates. Next, we will use the experiment to prove this result. The photocatalytic activities of $WO_3{\cdot}H_2O$ HMSs and $WO_3{\cdot}H_2O$ nanoplates on the degradation of RhB in aqueous solution were investigated, which is of great significance in environmental pollutant treatment. Figure 8a shows the optical absorption spectra of RhB aqueous solution with 50 mg of the $WO_3{\cdot}H_2O$ HMSs powder after exposure to visible light for different durations. The characteristic absorption peak of RhB at $\lambda = 553$ nm, and the area of the absorption peak correlates well with RhB concentration. It can be clearly seen that, with the increase of illumination time, the main absorption peak of RhB gradually weakened and no other absorption bands appear in either the ultraviolet or visible regions. Control experiments revealed that the photodegradation of RhB irradiated under visible light could almost be neglected in the absence of $WO_3{\cdot}H_2O$. Also, there was no appreciable degradation of RhB over the $WO_3{\cdot}H_2O$ HMSs after 6 h in the absence of visible light irradiation. Meanwhile, the RhB photodegraded by $WO_3{\cdot}H_2O$ nanoplates was also performed for comparison. As observed in Figure 8b, the $WO_3{\cdot}H_2O$ HMSs could degrade RhB by 94.8% within 5 h, but only less than 10% of RhB molecules are decomposed with nanoplates in the same period. Moreover, due to the low initial concentrations of the RhB ($C_0 = 10$ mg L^{-1}) and the photocatalytic degradation reaction is indeed pseudo-first-order, the linear relationship between $\ln c_0 / c$ and t can be fitted to the equation:

$$\ln c_0 / c = kt \qquad (1)$$

where c is the RhB concentration after irradiation time t, and k is the reaction rate constant. Figure 5c is intuitive summarized the linear relationship of two reactions. In this system, $k_{WO3{\cdot}H2O\ HMSs}$ is 0.5290 h^{-1} and $k_{WO3{\cdot}H2O\ nanoplates}$ is 0.0198 h^{-1}, which are summarized in Fig. 8c.

/Insert Figure 8/

To further investigate the mineralization degree of the organic compounds of $WO_3{\cdot}H_2O$ HMSs, the total organic carbon (TOC) experiment was performed. After the photocatalytic reaction continuous for 300 min, the TOC removal yields for RhB only 12% (Fig. S4). It means that $WO_3{\cdot}H_2O$ HMSs only can tear the attraction group of RhB under visible light, but can't effectively decompose the skeleton of RhB into inorganic carbon molecules, which is similar to that of TiO_2 under visible-light irradiation.[47,48]

Besides the activity, the stability of photocatalysts is equally important in practical applications. Therefore, the photoactivity of $WO_3{\cdot}H_2O$ HMSs was recycle-tested under visible light. As shown in Figure 8d, the hierarchical hollow microspheres photocatalysts did not exhibit any significant loss of activity after three recycles for the photodegradation of RhB, indicating that these photocatalysts are anti-photo corrosive during the photocatalytic oxidation of the dye molecules. The slight decline in the activity is mainly due to the loss of catalyst during the recycle experiment.

The toxicity of photocatalysts is also one of most important factor from the practical viewpoint. However, in the relevant reports, this indicator is often neglected. Thus, toxicity experiments for $WO_3{\cdot}H_2O$ HMSs were further investigated. The fungus plays a significant role in maintenance of ecological homeostasis, serving as decomposers of organic components to facilitate nutrient recycling and pollutant detoxification.[49] In our study, the yeast (*Saccharomyces cerevisiae*) was chosen because its cellular structure and functional organization has many similarities with cells of higher-level organisms and it has a short generation time and can be easily cultured.[50] From Figure S5, we can observed that $WO_3{\cdot}H_2O$ HMSs had not inhibited the yeast cells growth with the increased concentration to 1280 mg/L, which proves that the photocatalysts are nontoxic. More intuitive representation can be observed by fluorescein diacetate (FDA) staining technology, which is an ideal method to quantitatively measure the viability status of cells. Viable cells can esterase-catalyze hydrolysis non-fluorescent FDA, formation of a fluorescent product. As shown in Figure S6, after cultured 12 h with $WO_3{\cdot}H_2O$ HMSs, compared with blank, fluorescence still exists, and it means that $WO_3{\cdot}H_2O$ HMSs photocatalysts don't reduce the viability of the cells.

Proposed degradation mechanism of RhB

To monitor the active radicals that form during the photodegraded process, we first investigated the effect of band structure on the activity of the as-prepared $WO_3{\cdot}H_2O$ HMSs. We can calculate its conduction band (CB) bottom values and valence band (VB) top values through the following two equations 2 and 3:

$$E_{CB} = X - E_C - 1/2E_g \qquad (2)$$

$$E_{VB} = E_{CB} + E_g \qquad (3)$$

Where X is the absolute electronegativity of the semiconductor (For $WO_3{\cdot}H_2O$ is 6.885 eV).[46,51] E_C is the energy of free electrons on the hydrogen scale (~4.5 eV). E_g is the band gap energy of the semiconductor. Therefore, the CB and VB edges of $WO_3{\cdot}H_2O$ HMSs are ~1.26 and ~3.51 eV with respect to the NHE, respectively. In it, the potential of the holes at the VB is 1.52 eV higher than that of $^{\cdot}OH/OH^-$ (+1.99 eV), which meaning that the hole photogenerated on the surface of $WO_3{\cdot}H_2O$ HMSs could oxidize OH^- to $^{\cdot}OH$ from the theoretical viewpoint. To further confirm the presence of $^{\cdot}OH$, we measured the DMPO spin-trapping EPR spectra of $WO_3{\cdot}H_2O$ HMSs in aqueous dispersion of $WO_3{\cdot}H_2O$/RhB/DMPO. As displayed in Figure 7, there was no DMPO-$^{\cdot}OH$ signal can be detected before irradiation. After light illumination 30 min, it can be clearly observed characteristic four peaks of the DMPO-$^{\cdot}OH$ adduct with intensity 1 : 2 : 2 : 1, which confirming that $^{\cdot}OH$ generated during the $WO_3{\cdot}H_2O$ HMSs photodegradation of RhB.

/Insert Figure 9/

Generally speaking, photocatalytic activity is governed by various factors such as crystallinity, band gap, and surface properties. In this work, the photocatalytic superiority of the hierarchically $WO_3{\cdot}H_2O$ HMSs over the $WO_3{\cdot}H_2O$ nanoplates is easily understood. This is mainly attributed to the special structural features. The hierarchical nanostructure would effectively prevent nanoplates overlap and thus maintain a large active surface area ($WO_3{\cdot}H_2O$ HMSs: 23.21 m^2g^{-1}, $WO_3{\cdot}H_2O$ nanoplates: 14.01 m^2g^{-1}). The large surface area itself could harvest more visible light and then generate valence-band holes (h^+) and conduction-band electrons (e^-) pairs (reaction 4). The large number of h^+ could react with OH^- adsorbed on the catalyst surface to form highly reactive $^{\cdot}OH$, which could direct reaction of the organic pollutants with surface light energy (reaction 5-6).[52,53] In addition, the large surface area is favorable to increasing the catalytic reaction sites for the adsorption of reactant molecules and more surface OH^-, through the use of dissolved oxygen (O_2) (reaction 7-8). These surface OH^-, which not only could accept photogenerated holes to prevent h^+–e^- recombination, but also provide conditions for the subsequent production of $^{\cdot}OH$ (reaction 9), which is obviously beneficial for the enhancement of photocatalytic performance.[54]

$$WO_3{\cdot}H_2O + h\nu \rightarrow h^+ + e^- \quad (4)$$

$$h^+ + OH^- \rightarrow {\cdot}OH \quad (5)$$

$${\cdot}OH + h\nu + RhB \rightarrow \text{degrade products} \quad (6)$$

$$e^- + O_2 + H^+ \rightarrow H_2O_2 \quad (7)$$

$$H_2O_2 + e^- \rightarrow {\cdot}OH + OH^- \quad (8)$$

$$OH^- + h^+ \rightarrow {\cdot}OH \quad (9)$$

Besides, the unique hollow framework could also beneficial for the enhancement of photocatalytic performance. As is known to all, transport rate of the conduction band electrons on the surface of crystals is one of the critical aspects determining the overall reaction rate.[55,56] However, the rough surface of the crystal always acts as a barrier. Compared with dispersion of single nanoplates, hollow aggregating have more advantages in this respect. In order to generation hollow framework, inevitably leads to each single nanoplate of the microsphere arrange more closely and construct a relative continuous surface structure.[57] This point can be confirmed from the reduced of average pore size of two kinds $WO_3{\cdot}H_2O$ nanostructures ($WO_3{\cdot}H_2O$ HMSs: ~14 nm, $WO_3{\cdot}H_2O$ nanoplates: ~20 nm). Logically, this fact can facilitate efficient conduction band electron transportation, thereby promoting the photocatalytic performance.

4. Conclusions

In summary, we have successfully controlled the formation of hierarchical $WO_3 \cdot H_2O$ hollow microspheres based on the reaction system for preparing simple nanoplates. The formation mechanism of $WO_3 \cdot H_2O$ nanoplates and hierarchical $WO_3 \cdot H_2O$ HMSs has been discussed in detail. Visible light photocatalytic activity was produced, hierarchical hollow architecture materials could effectively reduce the band gap of $WO_3 \cdot H_2O$ and showed higher photocatalytic activity than $WO_3 \cdot H_2O$ nanoplates.

Acknowledgements

This work was supported by the National Science Foundation of China (no. 21271108), the Ministry of Science and Technology (Grant 2014CB932001), 2011 Science Foundation of Tianjin (No. 11JCZDJC24800), and China–U.S. Center for Environmental Remediation and Sustainable Development.

References

1 H. Cölfen and S. Mann, *Angew. Chem., Int. Ed.* 2003, **42**, 2350–2365.

2 M. A. Antonietti and G. Ozin, *Chem.–Eur. J.* 2004, **10**, 28–41.

3 H. Q. Yan, R. R. He, J. Johnson, M. Law, R. J. Saykally and P. D. Yang, *J. Am. Chem. Soc.* 2003, **125**, 4728–4729.

4 C. L. Nehl, H. W. Liao and J. H. Hafner, *Nano Lett.* 2006, **6**, 683–688.

5 Z. W. Pan, S. M. Mahurin, S. Dai and D. H. Lowndes, *Nano Lett.* 2005, **5**, 723–727.

6 A. Parfenov, I. Gryczynski, J. Malicka, C. D. Geddes and J. R. Lakowicz, *J. Phys. Chem. B* 2003, **107**, 8829–8833.

7 M. H. Cao, T. F. Liu, S. Gao, G. B. Sun, X. L. Wu, C. W. Hu and Z. L. Wang, *Angew. Chem., Int. Ed.* 2005, **44**, 4197–4201.

8 R. J. Waller, *Decision Sci.* 1976, **7**, 659–674.

9 G. A. A. Soler-lllia, C. Sanchez, B. Lebeau and J. Patarin, *Chem. Rev*. 2002, **102**, 4093–4138.

10 M. Heim, L. Römer and T. Scheibel, *Chem. Soc. Rev.* 2010, **39**, 156–164.

11 S. Q. Shang, X. L. Jiao and D. R. Chen, *ACS Appl. Mater. Interfaces* 2012, **4**, 860–865.

12 G. J. Ke, H. Y. Chen, C. Y. Su and D. B. Kuang, *J. Mater. Chem. A* 2013, **1**, 13274–13282.

13 M. Pradhan, A. K. Sinha and T. Pal, *RSC Adv.* 2014, **4**, 30315–30324.

14 Y. C. Jiang, S. D. Zhang, Q. Ji, J. Zhang, Z. P. Zhang and Z. Y. Wang, *J. Mater. Chem. A* 2014, **2**, 4574–4579.

15 D. E. Przybyla, C. M. R. Pérez, J. Gleaton, V. Nandwana and J. Chmielewski, *J. Am. Chem. Soc.* 2013, **135**, 3418–3422.

16 Y. S. Jun, E. Z. Lee, X. C. Wang, W. H. Hong, G. D. Stucky and A. Thomas, *Adv. Funct. Mater*. 2013, **23**, 3661–3667.

17 S. J. Ding, T. Zhu, J. S. Chen, Z. Y. Wang, C. l. Yuan and X. W. Lou (David), *J. Mater. Chem.* 2011, **21**, 6602–6606.

18 B. T. Zhu, Z. Y. Wang, S. J. Ding, J. S. Chen and X. W. Lou (David), *RSC Adv.* 2011, **1**, 397–400.

19 G. Q. Zhang, L. Yu, H. E. Hoster and X. W. Lou (David), *Nanoscale* 2013, **5**, 877–881.

20 L. N. Ye, W. Guo, Y. Yang, Y. F. Du and Y. Xie, *Chem. Mater*. 2007, **19**, 6331–6337.

21 X. X. Li, Y. J. Xiong, Z. Q. Li and Y. Xie, *Inorg. Chem*. 2006, **45**, 3493−3495.

22 L. Liu, H. J. Liu, H. Z. Kou, Y. Q. Wang, Z. Zhou, M. M. Ren, M. Ge and X. W. He, *Cryst. Growth Des.* 2009, **9**, 113–117.

23 C. S. Guo, G. Ming, L. Liu, G. D. Gao, Y. C. Feng and Y. Q. Wang, *Environ. Sci. Technol.* 2010, **44**, 419–425.

24 X. W. Lou (David) and L. A. Archer, *Adv. Mater.* 2008, **20**, 1853−1858.

25 X. Wang, M. Y. Liao, Y. T. Zhong, J. Y. Zheng, W. Tian, T. Y. Zhai, C. Y. Zhi, Y. Ma, J. N. Yao, Y. Bando and D. Golberg, *Adv. Mater.* 2012, **24**, 3421−3425.

26 S. Cheng, D. Yan, J. T. Chen, R. F. Zhuo, J. J. Feng, H. J. Li, H. T. Feng and P. X. Yan, *J. Phys. Chem. C* 2009, **113**, 13630−13635.

27 K. C. Kao, C. J. Tsou and C. Y. Mou, *Chem. Commun.* 2012, **48**, 3454−3456.

28 H. Q. Wang, M. Miyauchi, Y. Ishikawa, A. Pyatenko, N. Koshizaki, Y. Li, L. Li, X. Y. Li, Y. Bando and D. Golberg, *J. Am. Chem. Soc.* 2011, **133**, 19102−19109.

29 X. W. Lou David, Y. Wang, C. L. Yuan, J. Y. Lee and L. A. Archer, *Adv. Mater.* 2006, **18**, 2325−2329.

30 L. L. Li, Y. Chu, Y. Liu and L. H. Dong, *J. Phys. Chem. C* 2007, ***111***, 2123−2127.

31 A. Q. Pan, H. B. Wu, L. Yu and X. W. Lou (David), *Angew. Chem., Int. Ed.* 2013, **52**, 2226−2230.

32 Z. X. Wang, S. X. Zhou and L. M. Wu, *Adv. Funct. Mater.* 2007, **17**, 1790–1794.

33 S. Q. Guo, X. Zhang, Z. Zhou, G. D. Gao and L. Liu, *J. Mater. Chem. A* 2014, **2**, 9236–9243.

34 S. Q. Guo, X. Zhang, Z. W. Hao, G. D. Gao, G. Li and L. Liu, *RSC Adv.* 2014, **4**, 31353–31361.

35 G. C. Xi, J. H. Ye, Q. Ma, N. Su, H. Bai and C. Wang, *J. Am. Chem. Soc.* 2012, **134**, 6508–

6511.

36 Y. P. He and Y. P. Zhao, *J. Phys. Chem. C* 2008, **112**, 61–68.

37 Z. J. Gu, Y. Ma, W. S. Yang, G. J. Zhang and J. N. Yao, *Chem. Commun.* 2005, 3597–3599.

38 X. L. Li, T. J. Lou, X. M. Sun and Y. D. Li, *Inorg. Chem.* 2004, **43**, 5442–5449.

39 C. Santato, M. Odziemkowski, M. Ulmann and J. Augustynski, *J. Am. Chem. Soc.* 2001, **123**, 10639–10649.

40 J. M. Ma, J. Q. Yang, L. F. Jiao, Y. H. Mao, T. H. Wang, X. C. Duan, J. B. Lian and W. J. Zheng, *CrystEngComm* 2012, **14**, 453–459.

41 Y. P. He, Z. Y. Wu, L. M. Fu, C. R. Li, Y. M. Miao, L. Cao, H. M. Fan and B. S. Zou, *Chem. Mater.* 2003, **15**, 4039–4045.

42 J. M. Ma, D. N. Lei, X. C. Duan, Q. H. Li, T. H. Wang, A. M. Cao, Y. H. Mao and W. J. Zheng, *RSC Adv.* 2012, **2**, 3615–3617.

43 J. M. Ma, X. C. Duan, J. B. Lian, T. Kim, P. Peng, X. D. Liu, Z. F. Liu, H. B. Li and W. J. Zheng, *Chem.–Eur. J.* 2010, **16**, 13210–13217.

44 K. J. M. Bishop, C. E. Wilmer, S. Soh and B. A. Grzybowski, *Small* 2009, **5**, 1600–1630.

45 S. King, K. Hyunh and R. Tannenbaum, *J. Phys. Chem. B* 2003, **107**, 12097–12104.

46 Y. Liu, Q. Li, S. Gao and J. K. Shang, *CrystEngComm* 2014, **16**, 7493–7501.

47 Y. P. Huang, J. Li, W. H. Ma, M. M. Cheng, J. C. Zhao, *J. Phys. Chem. B* 2004, **108**, 7263–7270.

48 C. C. Chen, W. Zhao, J. Li, J. C. Zhao, *Environ. Sci. Technol*. 2002, **36**, 3604–3611.

49 Q. L. Yu, M. Q. Sun, Y. M. Wang, C. Li and L. Liu, *RSC Adv.* 2014, **4**, 20371–20378.

50 K. Kasemets, A. Ivask, H. Dubourguier and A. Kahru, *Toxicology in Vitro* 2009, **23**, 1116–1122.

51 R. G. Pearson, *Inorg. Chem.* 1988, **27**, 734–740.

52 Y. H. Lv, Y. Y. Liu, Y. Y. Zhu and Y. F. Zhu, *J. Mater. Chem. A* 2014, **2**, 1174–1182.

53 D. Liu, Y. H. L, M. Zhang, Y. F. Liu, Y. Y. Zhu, R. L. Zong and Y. F. Zhu, *J. Mater. Chem. A*

2014, **2**, 15377–15388.

54 S. X. Ge, H. M. Jia, H. X. Zhao, Z. Zheng and L. Z. Zhang, *J. Mater. Chem.* 2010, **20**, 3052–3058.

55 M. R. Hoffmann, S. T. Martin, W. Choi and D. W. Bahnemann, *Chem. Rev.* 1995, **95**, 69 – 96.

56 A. Kubacka, M. Fernandez-Garcia and G. Colon, *Chem. Rev.* 2012, **112**, 1555 – 1614.

57 Y. B. Zhao, Q. F. Chen, F. Pan, H. Li, G. Q. Xu and W. Chen, *Chem.–Eur. J.* DOI: 10.1002/chem.201400120.

Figure Captions

Figure 1. a, b) Field-emission scanning electron microscopy (FESEM) of $WO_3 \cdot H_2O$ nanoplates, c) HRTEM image, d) XRD patterns.

Figure 2. a) Schematic diagram of WO_6 octahedron in $WO_3 \cdot H_2O$, b) Schematic description of the 2D layer plane (left) and 2D $4^4 \cdot 6^2$ net (right), c) the O–H/O stacking interactions between adjacent 2D layer planes.

Figure 3. a, b) Field-emission scanning electron microscopy (FESEM) of $WO_3 \cdot H_2O$ hollow microspheres (HMSs), c, d) transmission electron microscopy (TEM), e) XRD patterns, f) N_2 adsorption/desorption isotherm and Barrett-Joyner-Halenda (BJH) pore size distribution plot (inset) of $WO_3 \cdot H_2O$ HMSs.

Figure 4. SEM images of samples synthesized with different molar ratio of $Na_2WO_4 \cdot 2H_2O$ to citric acid: a) 1: 1, b)1: 1.25, c) 1: 1.5, d) 1: 1.75, e) 1: 2.

Figure 5. SEM images of the samples synthesized at 100 °C for a) 1 h, b) 2 h, c) 4 h, and d) XRD patterns of the as-prepared $WO_3 \cdot H_2O$ products.

Figure 6. a) UV-vis diffuse reflectance and b) emission spectra of $WO_3 \cdot H_2O$ HMSs and $WO_3 \cdot H_2O$ nanoplates.

Figure 7. Nyquist plots of the dummy cell fabricated with $WO_3 \cdot H_2O$ HMSs and $WO_3 \cdot H_2O$ nanoplates.

Figure 8. a) Absorption spectra of a solution of RhB in the presence of $WO_3 \cdot H_2O$ HMSs and under exposure to visible light, (b) time course of the decrease in the dye concentration using different catalysts, (c) corresponding selected fitting results using pseudo-first-order reaction kinetics. (d) Cycling runs in the photocatalytic degradation of RhB by $WO_3 \cdot H_2O$ HMSs products.

Figure 9. EPR spectra of DMPO-$\cdot$OH adducts for $WO_3 \cdot H_2O$/RhB dispersion in water.

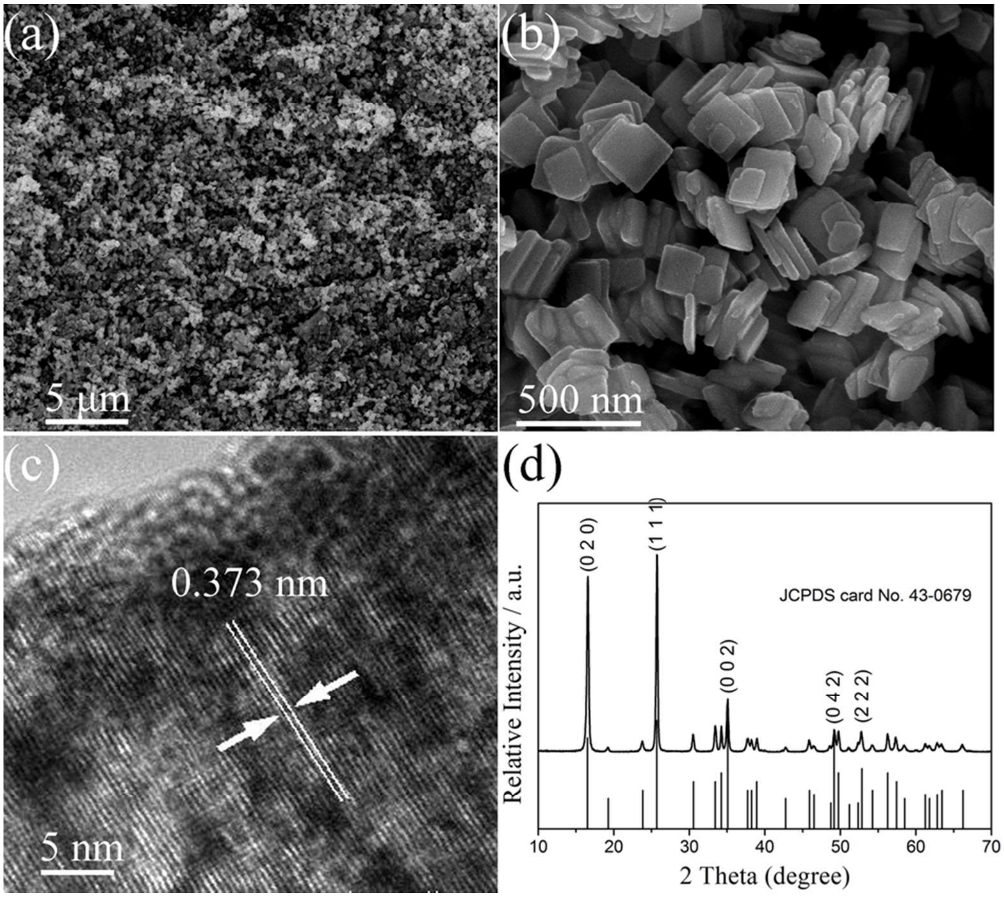

Figure 1. a, b) Field-emission scanning electron microscopy (FESEM) of $WO_3 \cdot H_2O$ nanoplates, c) HRTEM image, d) XRD patterns.
80x71mm (300 x 300 DPI)

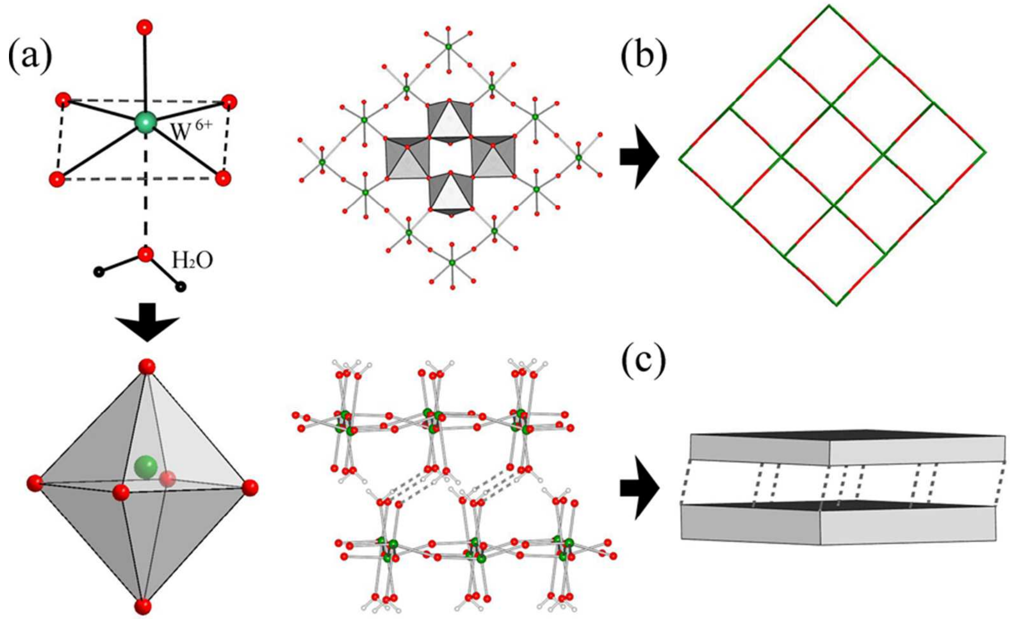

Figure 2. a) Schematic diagram of WO6 octahedron in WO3·H2O, b) Schematic description of the 2D layer plane (left) and 2D 44·62 net (right), c) the O–H/O stacking interactions between adjacent 2D layer planes.
80x49mm (300 x 300 DPI)

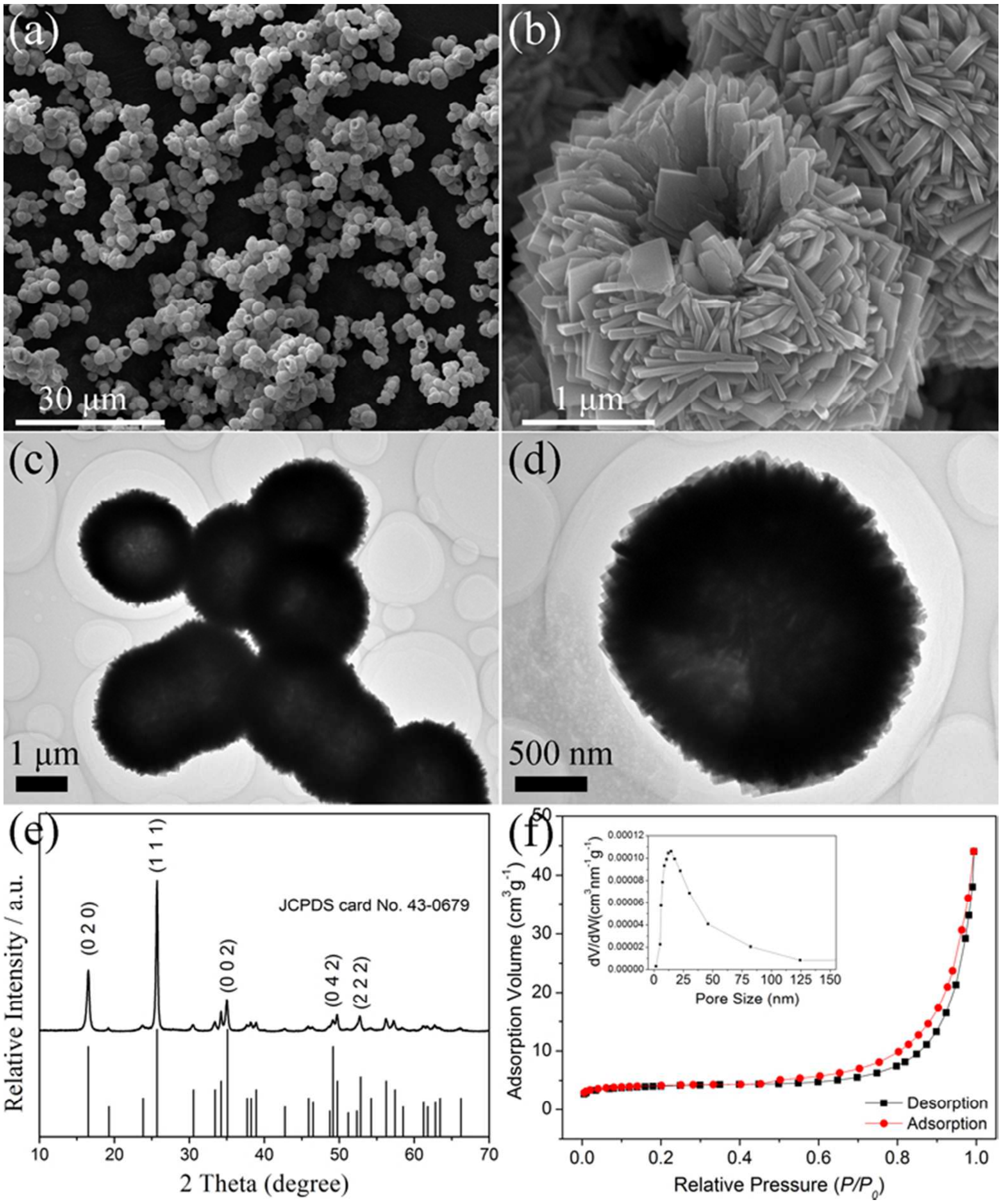

Figure 3. a, b) Field-emission scanning electron microscopy (FESEM) of WO3·H2O hollow microspheres (HMSs), c, d) transmission electron microscopy (TEM), e) XRD patterns, f) N2 adsorption/desorption isotherm and Barrett-Joyner-Halenda (BJH) pore size distribution plot (inset) of WO3·H2O HMSs.
66x80mm (300 x 300 DPI)

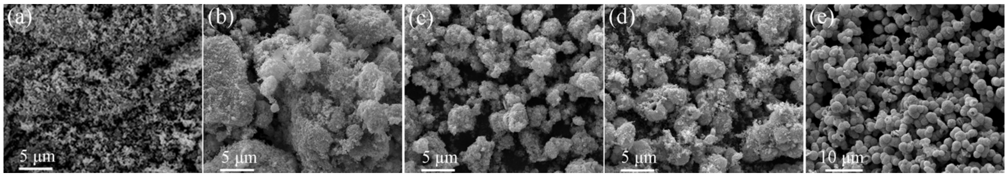

Figure 4. SEM images of samples synthesized with different molar ratio of $Na_2WO_4 \cdot 2H_2O$ to citric acid: a) 1: 1, b)1: 1.25, c) 1: 1.5, d) 1: 1.75, e) 1: 2.
140x23mm (300 x 300 DPI)

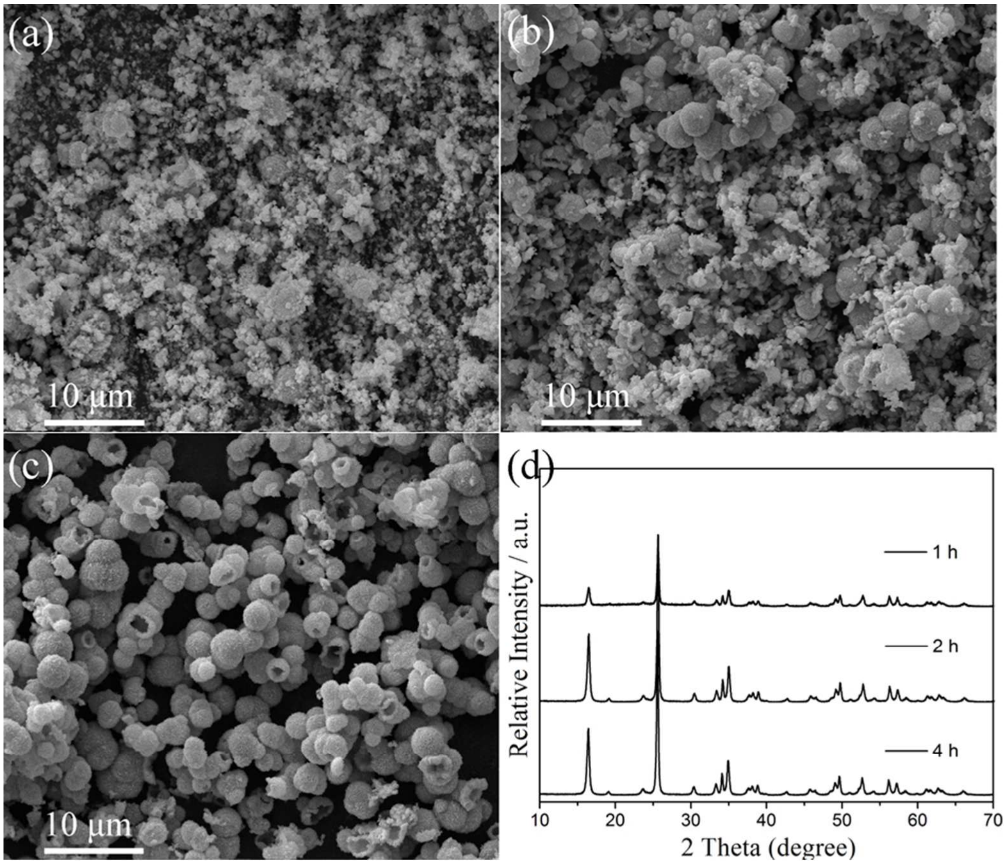

Figure 5. SEM images of the samples synthesized at 100 °C for a) 1 h, b) 2 h, c) 4 h, and d) XRD patterns of the as-prepared $WO_3 \cdot H_2O$ products.
80x68mm (300 x 300 DPI)

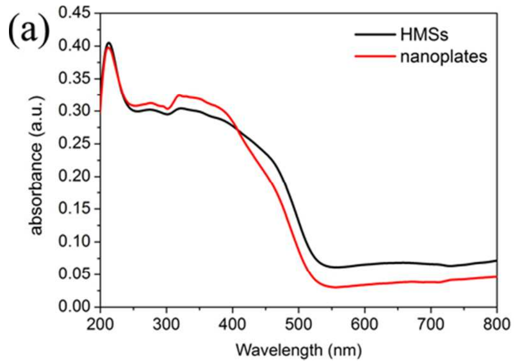

Figure 6. a) UV-vis diffuse reflectance and b) emission spectra of $WO_3 \cdot H_2O$ HMSs and $WO_3 \cdot H_2O$ nanoplates.
80x28mm (300 x 300 DPI)

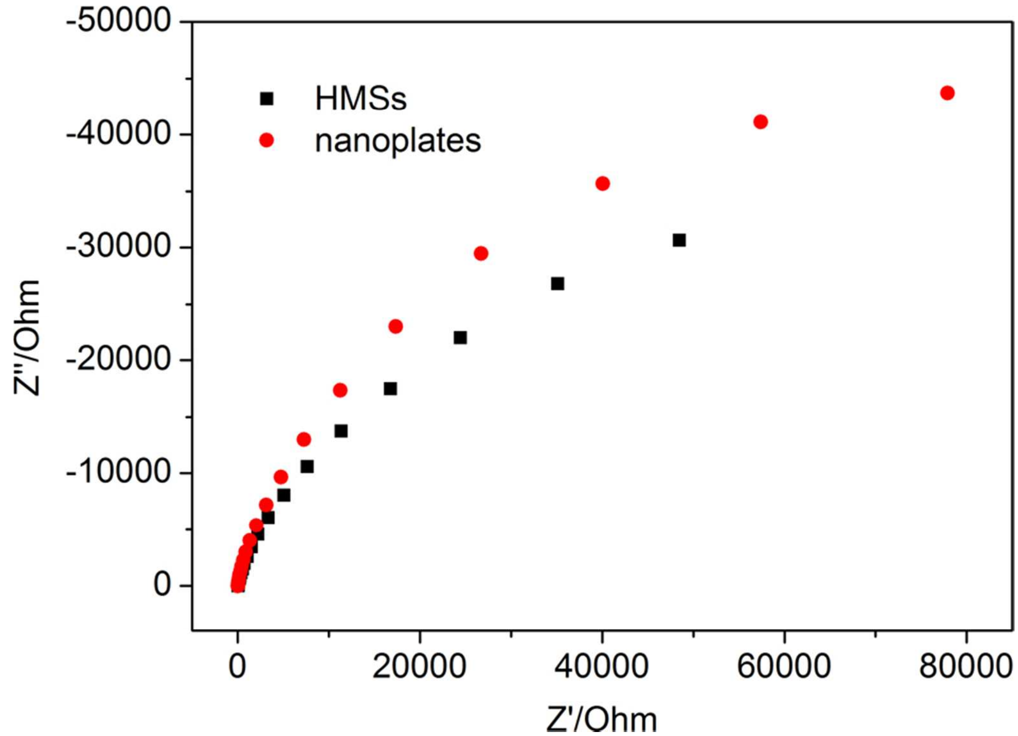

Figure 7. Nyquist plots of the dummy cell fabricated with WO3·H2O HMSs and WO3·H2O nanoplates.
80x58mm (300 x 300 DPI)

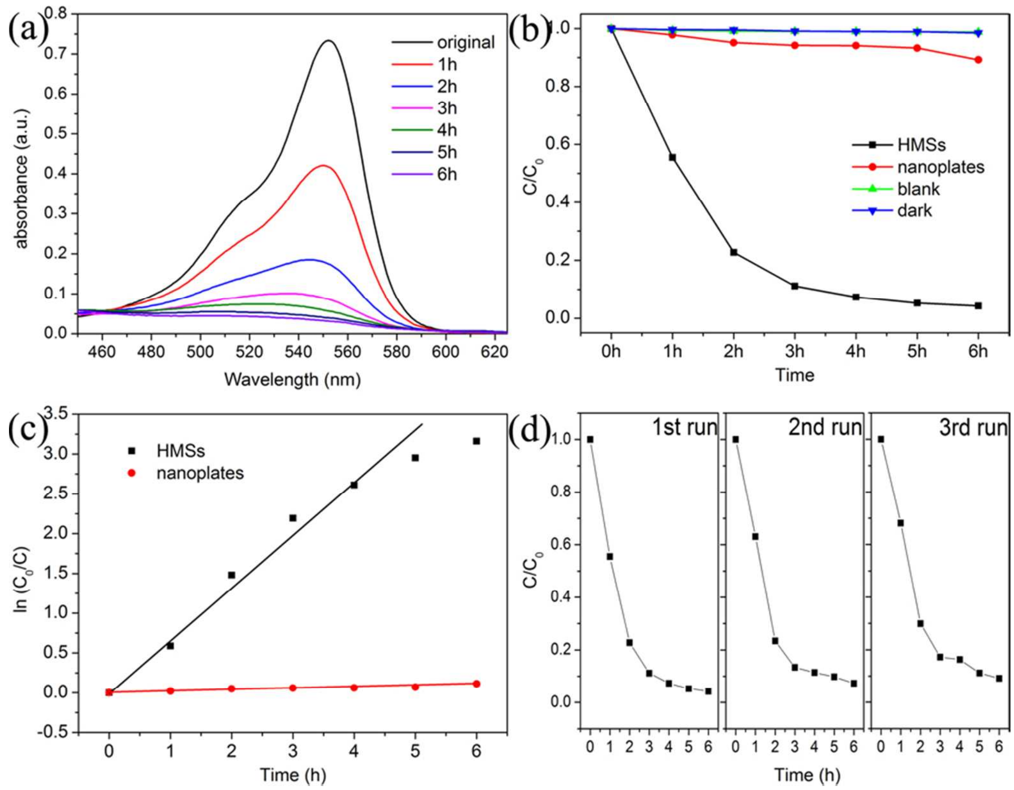

Figure 8. a) Absorption spectra of a solution of RhB in the presence of WO3·H2O HMSs and under exposure to visible light, (b) time course of the decrease in the dye concentration using different catalysts, (c) corresponding selected fitting results using pseudo-first-order reaction kinetics. (d) Cycling runs in the photocatalytic degradation of RhB by WO3·H2O HMSs products.
80x62mm (300 x 300 DPI)

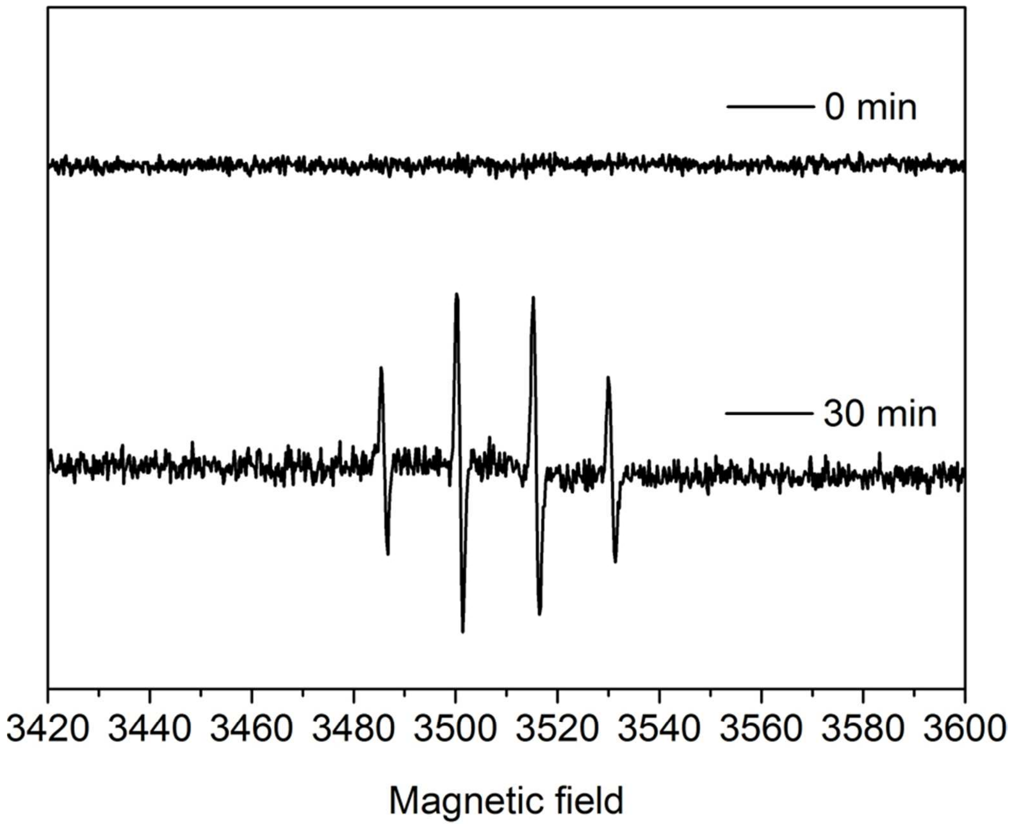

80x65mm (300 x 300 DPI)